

## Improved E-modulus-reconstruction by considering the spatially non-stationary errors of ultrasonic displacement estimation

A. Eder<sup>1</sup>, M. Richter<sup>2</sup>, and Ch. Kargel<sup>1</sup>

<sup>1</sup>Department of Electrical Engineering and Information Technology,  
Bundeswehr University Munich/ Division of Sensor Technology and Measurement Systems,  
Neubiberg/Munich, Germany

<sup>2</sup>Department of Electrical Engineering and Information Technology,  
Bundeswehr University Munich / Division of Mathematics,  
Neubiberg/Munich, Germany

---

Copyright © 2014 ISSR Journals. This is an open access article distributed under the *Creative Commons Attribution License*, which permits unrestricted use, distribution, and reproduction in any medium, provided the original work is properly cited.

**ABSTRACT:** Ultrasound elastography is a promising imaging modality for the differentiation between benign and malignant tissue, such as the detection of stiff tumors in the (female) breast. In order to deduce the elastic tissue properties and reconstruct the spatial distribution of Young's modulus (E-modulus), the inverse problem governed by the equilibrium equations of linear elastostatics must be solved using internal tissue displacement estimates which are, in practice, subject to spatially non-stationary measurement errors.

In this paper we investigate the novel E-modulus reconstruction approach of taking into account the spatially non-stationary errors of ultrasonic displacement estimates within the field-of-view. The application of spatially adaptive weight factors derived from the mean-square displacement estimation errors by means of an appropriate confidence measure leads to an improved reconstruction quality that strikes the best balance between the two opposing reconstruction goals of "achieving high image homogeneity" and "keeping high-frequency spatial information", which both are diagnostically important. We demonstrate that over- and under-regularization within the field-of-view can be significantly reduced leading to an improved image quality. The results presented here are derived from extensive simulations and phantom experiments. The simulation results will be compared to those of an earlier study.

**KEYWORDS:** Ultrasound, elastography, displacement estimation, measurement errors, inverse problem, reconstruction.

### 1 INTRODUCTION

The improvement of the sensitivity and specificity of medical imaging methods is of paramount diagnostic interest because the early detection and treatment of cancer is crucial for the survival rate. A promising imaging method is elastography, which just like manual palpation makes use of the fact that tumors often show an increased stiffness compared to the surrounding healthy tissue [2]. The measured response, i.e. the internal tissue displacements, of e.g. breast tissue to a mechanical stimulus is utilized to determine the spatial distribution of mechanical (elastic) tissue properties like Young's modulus (E-modulus). Even small tumors which are not located close to the skin surface might be detected because elastography is not restricted by the limited human tactile abilities to sense stress and strain. In practice, two medical imaging modalities – ultrasound (US) and magnetic resonance imaging (MRI) – are applied and several static and dynamic elastography approaches exist [3–8]. Medical US examinations do not pose health risks and compared to MRI can be easily performed at the bedside, are cost effective and widely available even in rural areas.

In ultrasound elastography – first proposed in the early 1990s [3] – soft breast tissue is objected to a (uniaxial) compression force which is applied externally using the transducer of a medical ultrasound scanner. Ultrasound echo data is

acquired from the tissue before and after quasi-static compression steps and one, two or even all three components of the internal tissue displacement vectors are determined using suitable displacement estimation methods [9–12]. In the original approach the two-dimensional (2D) spatial distribution of the axial (defined as the direction of compression and ultrasound wave propagation) strain is derived from the gradient of the estimated axial displacement estimates [13] and displayed as a qualitative (inverse) measure for the E-modulus distribution in the tissue as a so-called strain image. The principle diagnostic benefit of strain imaging was demonstrated in several studies (e.g. [4], [14]). Nevertheless, the interpretation of the internal strain distribution as a measure for the E-modulus has certain drawbacks, such as the amplification of high-frequency displacement estimation noise requiring methods with low displacement estimation variance [15]. Another serious drawback is the necessary assumption of a uniform stress distribution throughout the observed tissue region. Since this uniformity condition can hardly be met in an *in-vivo* situation, there may be substantial strain image artifacts and diagnostic misinterpretations.

A more sophisticated approach is the reconstruction of the spatial E-modulus distribution from the internal displacement distribution using elasto-mechanic models based on the generalized Hooke's law [16]. Although this model-based approach incorporates serious problems like the unknown *in-vivo* boundary conditions and the general ill-posedness of the inverse problem to be solved, several groups have successfully developed reconstruction approaches using one, two or even three components of estimated displacement vectors (e.g. in [11, 17–19]). The inverse reconstruction problem is generally formulated as regularized nonlinear optimization problem, where a finite element method (FEM) [20] is applied in order to solve the forward problem, i.e. calculating the internal displacement vectors for a particular spatial E-modulus distribution and a given set of mechanical boundary conditions.

In practice, noise-free displacement data is not available. In order to achieve reconstruction results (elastograms) with a quality sufficient for diagnostic purposes, regularization of the optimization problem using an appropriate regularity measure must thus be introduced. However, the applied regularization inevitably induces a loss of high-frequency spatial information, which might be diagnostically important. For example, sharp edges between soft healthy tissue and an inclusion with increased E-modulus in an elastogram might be evidence for an *in-situ* rather than an invasive carcinoma [2]. For a high diagnostic value of the reconstruction results, regularization must optimally balance the conflicting goals of reducing the negative influences of displacement estimation errors and achieving high spatial resolution in elastograms. Under-regularized (i.e. the influences of the displacement estimation errors degrade the elastogram homogeneity) or over-regularized (i.e. the regularization leads to an unnecessary loss of high-frequency spatial information) elastograms are clearly suboptimal.

Finding the best amount of regularization is not straightforward because the displacement estimation errors have different magnitudes in axial, lateral and elevational direction and they have a non-stationary (or at best cyclo-stationary) character within the field of view (FOV) of the ultrasound transducer. For example, the signal-to-noise-ratio (SNR) of the echo signals in a typical breast-ultrasound examination can easily change by up to 30 dB within the FOV. Depending on the displacement estimators applied, this may lead to displacement estimation variances that spatially differ in the FOV by several hundred percent.

Richards et al. [11] have recently proposed the use of 3 different - but constant - weight factors in the reconstruction for the axial, lateral and elevational displacement components in order to account for the different displacement estimation variances in the respective directions. This approach does not solve the problem that is caused by the spatially varying displacement estimation variances such that within the FOV there are still regions where the reconstruction result is under-regularized or over-regularized.

In this paper we propose a 2D reconstruction approach with adaptive weight factors for the axial and lateral displacement estimates that fully takes into consideration the non-stationary displacement estimation errors. The adaptive weight factors are derived based upon a confidence measure for the displacement estimates.

## 2 METHODS

### 2.1 DISPLACEMENT ESTIMATION

Subjecting a material to a small external compression force leads to a deformation, where each point inside the material defined by its Cartesian coordinates  $\mathbf{x} = [x, y, z]^T$  is shifted by a displacement vector  $\mathbf{u} = \mathbf{u}(x, y, z) = [u_x, u_y, u_z]^T$  to its new position  $\mathbf{x}' = \mathbf{x} + \mathbf{u}$ . The resulting displacement vector field  $\mathbf{u}$  for a linear-elastic material is thereby given by the generalized Hooke's law in 3D.

Different algorithms for the estimation of internal tissue displacement vectors using ultrasound echo signals have been proposed and described in literature for the estimation of axial,  $u_z$  [3] [9] [12], axial and lateral ( $u_z, u_x$ ) [10] [19] [21] and even all three [11] components of the displacement vector  $\mathbf{u}$ .

For the estimation of the axial  $u_z$  and lateral  $u_x$  displacement vector components we use block-matching [4] applied to the envelopes of the pre-compressed  $A[n, m]$  and postcompressed  $A'[n, m]$  digital ultrasound echo signals. The best match, as depicted in principle in Fig. 1, of a small block (= envelope data from a small tissue region) of the pre-compressed envelope data (i.e. template block,  $T[k, \ell] \in A[n, m]$  with  $k = 1 \dots K$  and  $\ell = 1 \dots L$ ) is to be found in a certain region of the post-compressed envelope data (i.e. search region,  $S[i, j] \in A'[n, m]$  with  $i = 1 \dots I$  and  $j = 1 \dots J$ ).

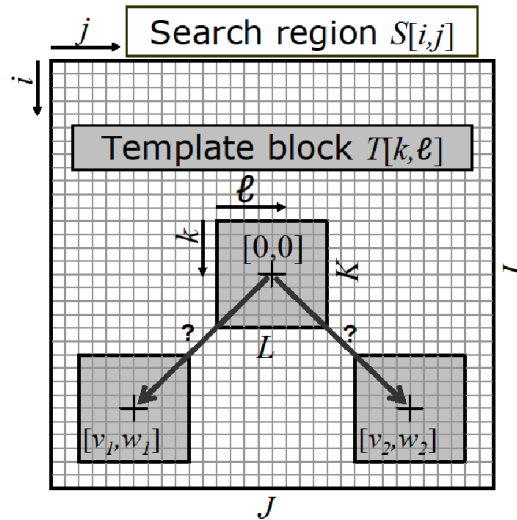


Fig. 1. Principle of 2D block-matching, with the template block  $T[k, \ell]$  for which the best-match is to be found within the search region  $S[i, j]$ .

The best-match of  $T$  in  $S$  is indicated by the extremum of the matching-function  $f_{MF}[v, \omega]$  using  $T[k, \ell]$  and  $S[i, j]$ . For the investigations shown in this paper we chose the mean-squared-differences (MSD) function for  $f_{MF}[v, \omega]$  [4]:

$$f_{MF}[v, \omega] = \frac{1}{KL} \sum_{k=1}^K \sum_{\ell=1}^L (T[k, \ell] - S[k + v, \ell + \omega])^2 \tag{1}$$

where  $v = 0 \dots I - K$  and  $\omega = 0 \dots J - L$ . The 2D displacement estimate  $\hat{\mathbf{u}}$  for the tissue region represented by  $T[k, \ell]$  is then determined from the location of the minimum of  $f_{MF}[v, \omega]$ :

$$\hat{\mathbf{u}} = [\hat{u}_z, \hat{u}_x]^T = \arg \min \{ f_{MF}[v, \omega] \} \tag{2}$$

For the E-modulus reconstruction, spatial resolutions in the sub-sample range are needed for the axial and lateral displacement estimates because most commercial ultrasound scanners provide echo signal sampling rates of approximately 30-40 MS/s. To achieve this goal, a polynomial fitting function  $f_{Fit}(z, x)$  of 2<sup>nd</sup> order in the 2 variables  $z$  (axial) and  $x$  (lateral) is used to approximate the matching function:

$$f_{Fit}(z, x) = a_0 + a_1z + a_2x + a_3zx + a_4z^2 + a_5x^2 \tag{3}$$

In order to find the coefficients of the polynomial function that fits best to  $f_{MF}[\nu, \omega]$ , an equation system deduced from at minimum 6 full-sample values of  $f_{MF}[\nu, \omega]$  including the full-sample minimum is solved in a least-squares sense using the pseudo-inverse matrix. The location of the minimum  $[z_{min}, x_{min}]^T$  of the resulting  $f_{Fit}(z, x)$  is then calculated analytically in order to determine the displacement estimate  $\hat{\mathbf{u}}$  with sub-sample resolution.

According to the definition of  $f_{MF}[\nu, \omega]$ , the minimum  $f_{Fit}(z_{min}, x_{min})$  is an estimate for the mean-square-error between the template block  $T[k, \ell]$  and the search region  $S[i, j]$ , and thus an indicator for the quality of the displacement estimate (i.e. the displacement estimation error). In order to obtain an applicable confidence measure  $C$  for each displacement estimate,  $f_{Fit}(z_{min}, x_{min})$  is normalized using the signal power of  $T[k, \ell]$ :

$$C = \frac{f_{Fit}(z_{min}, x_{min})}{\frac{1}{K \cdot L} \sum_{k=1}^K \sum_{\ell=1}^L T^2[k, \ell]} \quad (4)$$

$C$  will later be utilized to estimate the displacement estimation error, which in turn is used to calculate the adaptive weight factors for the E-modulus reconstruction (see section 4.3).

## 2.2 E-MODULUS RECONSTRUCTION

The E-modulus distribution which is sought within a field of view  $\Omega \subset \mathbb{R}^d$  can be mathematically described as a function  $E : \Omega \rightarrow \mathbb{R}$ , where  $d = 2$  in the two-dimensional case considered here. Since there is no method available to measure  $E$  directly, it needs to be inferred from internal tissue displacements (e.g. when the tissue is subjected to an external compression). The relationship between applied mechanical stress and resulting mechanical strain (and vice versa) is given by Hooke's law, which for homogenous, isotropic and linear elastic material can be simplified and written in tensor notation as follows [14]:

$$\sigma_{ij} = 2\mu\varepsilon_{ij} + \lambda\delta_{ij} \left( \sum_{k=1}^d \varepsilon_{kk} \right), \quad i, j = 1, \dots, d. \quad (5)$$

Here,  $\sigma_{ij}$  and  $\varepsilon_{ij}$  are the second order symmetric stress and strain tensors and  $\delta_{ij}$  is Kronecker's delta. The strain tensor  $\varepsilon_{ij}$  is calculated from the internal displacement  $\mathbf{u}$  by [14]:

$$\varepsilon_{ij} = \frac{1}{2} \left( \frac{\partial u_i}{\partial x_j} + \frac{\partial u_j}{\partial x_i} \right) \quad (6)$$

Note that the indices 1 or z and 2 or x are used interchangeably in order to designate axial and lateral components of  $\mathbf{u}$  and  $\varepsilon_{ij}$ , respectively. For example in (6),  $\varepsilon_{zz} = \partial u_z / \partial z$  can also be used to express the plane strain in axial direction.

Further,  $\mu$  and  $\lambda$  are the Lamé coefficients, which are related to the E-modulus via Poisson's ratio  $\nu$  as follows:

$$\mu = \frac{E}{2(1 + \nu)}, \quad (7)$$

$$\lambda = \frac{Ev}{(1+\nu)(1+2\nu)}. \tag{8}$$

Following e.g. Kallel *et al.* [17] in relaxing the incompressibility condition for soft tissue, Poisson’s ratio is set to a constant value of  $\nu = 0.495$ .

For static equilibrium,  $\sigma_{ij}$  must fulfill:

$$\sum_{j=1}^d \frac{\partial \sigma_{ij}}{\partial x_j} + f_i = 0, \quad i = \ell, \dots, d, \tag{9}$$

with  $f_i$  being the body forces associated to gravity. For small deformations,  $f_i$  may and will be neglected.

(9) is a system of second order elliptic partial differential equations for  $\mathbf{u} : \Omega \rightarrow \mathbb{R}^d$ . For a given  $E$  and additionally at the boundary of  $\Omega$  given either displacements  $\mathbf{u}$  (so-called Dirichlet boundary conditions) or external compression forces (so-called Neumann boundary conditions), system (9) may be solved for  $\mathbf{u}$ . In fact, both types of boundary conditions usually coexist on disjoint components of the boundary. Assuming fixed boundary conditions, solving (9) for given  $E$  yields a mapping  $E \mapsto \mathbf{u}$ . Computing  $\mathbf{u}$  from  $E$  is called the “forward problem”.

Since the forward problem can not be solved analytically, one must turn to numerical approximation. We choose to approximate  $E$  by a piecewise constant function on a uniform rectangular grid with mesh sizes  $h_z$  and  $h_x$ , comprising  $n_z$  grid points in axial and  $n_x$  grid points in lateral direction (including grid points on the boundary of  $\Omega$ ). Thus, the approximation is defined by  $m = (n_x - 1)(n_z - 1)$  nonnegative function values. These  $m$  values are assembled into a vector and the notation  $E$  is reused to designate it such that  $E \in \mathbb{R}_+^m$ .  $\mathbf{u}$  is approximated on the same grid by a piecewise bilinear vector field, i.e. bilinear scalar functions for both, axial ( $u_z$ ) and lateral ( $u_x$ ) displacements. This piecewise linear vector field can be represented by  $d \cdot n$  nodal values, where  $n = n_x n_z$ . From now on,  $\mathbf{u} \in \mathbb{R}^{dn}$  refers to this vector of nodal values. Finally, the approximate solution of (the weak form of) (9) by the finite element method means to solve the linear system of equations [20]:

$$K\mathbf{u} = F \tag{10}$$

with so-called stiffness matrix  $K$  and load vector  $F$ . Since both  $K$  and  $F$  depend on  $E$ , the solution of (10) ultimately defines a nonlinear mapping  $\Phi : \mathbb{R}_+^m \rightarrow \mathbb{R}^{dn}$ ,  $E \mapsto \Phi(E) = \mathbf{u}$ .

$E$  is not available in practice. However, from ultrasound echo data acquired from the tissue before and after compression (see section 2.1) estimates  $\hat{\mathbf{u}}$  of the actual displacements  $\mathbf{u}$  can be derived and one could now ask for a solution of the “inverse problem”: find  $E$  such that  $\Phi(E) = \hat{\mathbf{u}}$ . But even if the solution of this system of nonlinear equations existed, it would hardly be useful in practice because every displacement estimation method involves an estimation error. Regularization theory [22, 23] now suggests to find  $E = E_\rho$  as the solution of

$$E_\rho = \arg \min \{ G_\rho(E); E \in \mathbb{R}_+^m \} \text{ with} \tag{11}$$

$$G_\rho(E) = \left\| W \cdot (\Phi(E) - \hat{\mathbf{u}}) \right\|_2^2 + \rho R(E).$$

Here,  $G_\rho(E)$  is the cost-function which is to be minimized and  $W$  is a  $dn$ -dimensional diagonal matrix of positive weight factors  $W_i$ .  $\left\| W(\Phi(E) - \hat{\mathbf{u}}) \right\|_2^2$  measures “data fidelity” of  $E$ : the smaller the quadratic  $L_2$ -norm  $\left\| W(\Phi(E) - \hat{\mathbf{u}}) \right\|_2^2$  is, the better the reconstructed  $E$  “fits” to the measured displacements  $\hat{\mathbf{u}}$ . Every single measurement can be treated individually: the larger a specific weight factor  $W_i$  (component of  $W$ ) in relation to other weight factors is, the more importance gets attributed to

$\Phi_i(E)$  being close to the specific measurement  $\hat{\mathbf{u}}_i$  ( $i$ th component of  $\hat{\mathbf{u}}$ ). Specifically, we choose  $W_i$  depending on the root-mean-square-error  $\delta_{\Delta\hat{\mathbf{u}}_i}$  (also see (18)) for the displacement estimates  $\hat{\mathbf{u}}_i$

$$W_i = 1 / \delta_{\Delta\hat{\mathbf{u}}_i}, \quad i = 1, \dots, d \cdot n \tag{12}$$

forcing an optimal  $E_\rho$  that approximates the measured displacement values  $\hat{\mathbf{u}}$  the better, the more reliable they are in the sense of  $\delta_{\Delta\hat{\mathbf{u}}_i}$  being small. (12) means that weight factors are inverse measures of how much the measurement of  $\hat{\mathbf{u}}_i$  can be trusted. The better a measurement value  $\hat{\mathbf{u}}_i$  is, the more we will strive to reproduce it.

$R(E) \geq 0$  measures “regularity” of the reconstructed  $E$ , which becomes smaller with increasing similarity of  $E$  with some meaningful *a-priori* notion of it. As proposed in [11] and by others, we quantify the regularity of a continuously differentiable ( $\nabla$  denotes the Nabla operator) function  $f : \Omega \rightarrow \mathbb{R}$  by its total variation

$$\tau(f) = \int_{\Omega} \left\| \nabla f(x) \right\|_2 dx = \int_{\Omega} \sqrt{\nabla f(x) \cdot \nabla f(x)} dx \tag{13}$$

Here, the total variation  $\tau(E)$  of an  $E$ -modulus  $E : \Omega \rightarrow \mathbb{R}$  is approximated using its approximate representation  $E \in \mathbb{R}^m$  by

$$R(E) := \sum_i h^{d-1} \sqrt{\sum_{i_j} (E_{i_j} - E_i)^2 + h^2 \beta^2} \tag{14}$$

$\beta$  is a small positive number, which is introduced to make  $R(E)$  a differentiable function of  $E \in \mathbb{R}^m$ . The gradient  $\nabla E$  of function  $E$  is approximated by finite differences based on the discrete approximated values  $E \in \mathbb{R}^m$ . Thus,  $\sum_{i_j}$  means summation over one lateral and one axial neighbor element of  $E_i$ . Furthermore, for ease of notation  $h = h_x = h_z$  has been used in (14). In practice,  $h_x$  and  $h_z$  may differ.

Finally,  $\rho$  determines the mutual importance of “data fidelity” versus “regularity” when seeking a minimum of  $G_\rho(E)$  (see (11)). In the one extreme case  $\rho = 0$ , there is no regularization at all and only the weighted squared differences between  $\Phi_i(E)$  and  $\hat{\mathbf{u}}$  are to be minimized. In the other extreme case  $\rho = \infty$ , a perfectly regular  $E$  - not at all affected by the measurements  $\hat{\mathbf{u}}$  - will result.

The iterative approach applied here in order to find  $E_\rho$  is illustrated as a block diagram in Fig. 2.

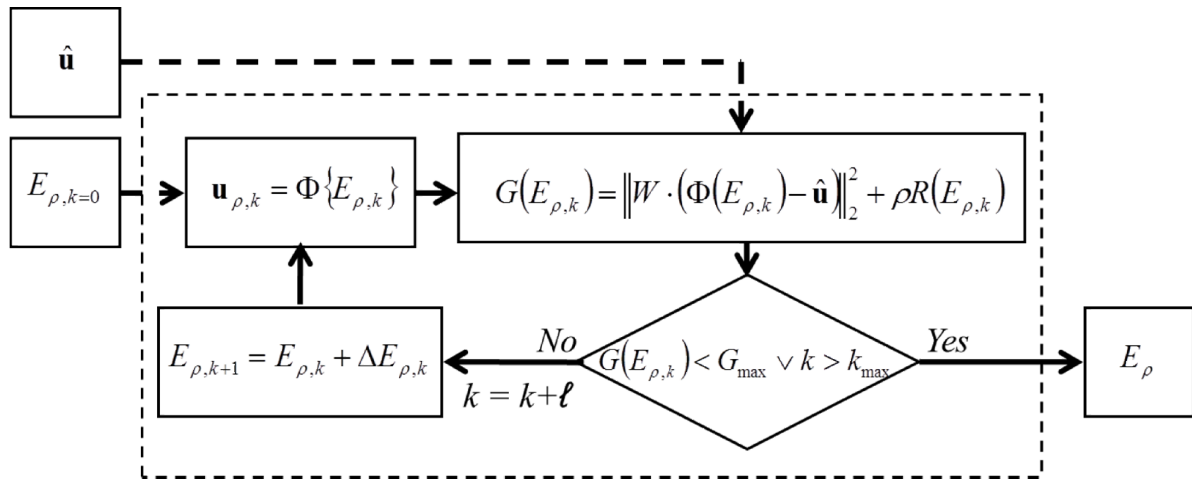


Fig. 2. Block diagram of the E-modulus reconstruction.

According to Fig. 2 the iteration is terminated if a maximum of  $k_{max}$  steps is exceeded. Additional termination conditions (not explicitly listed) are an insufficient relative decrease in the value of  $\|G(E)\|_2^2$  between two iterates and an insufficient change  $\|E_k - E_{k-1}\|_2$ . In order to determine the search direction  $\Delta E_k$ , Gauss-Newton type algorithms - like the one implemented in Matlab's iterative solver *lsqnonlin* - require computation of  $\Delta G(E) \cdot \mathbf{v}$  and  $\Delta G(E)^T \cdot \mathbf{v}$  for vectors  $\mathbf{v} \in \mathbb{R}^m$ , where  $\Delta G(E)$  is the Jacobian of  $G(E)$ . We achieve computation of  $\Delta G(E) \cdot \mathbf{v}$  in a way similar to the "adjoint method" described in [18].

For a numerical solution of (11), we relied on MATLAB's function *lsqnonlin* which employs a trust region Newton method and requires (11) to be cast into the equivalent form

$$E_\rho = \arg \min \left\{ \left\| W(\Phi(E) - \mathbf{u}); \sqrt{\rho \mathbf{R}\{E\}} \right\|_2^2 \right\} \tag{15}$$

where  $\mathbf{R}\{E\}$  is a vector with  $i^{\text{th}}$  component

$$\mathbf{R}_i\{E\} = \left( \sum_{i_j} (E_i - E_{i_j})^2 + h^2 \beta^2 \right)^{0.25} \tag{16}$$

### 3 DISPLACEMENT ESTIMATION SIMULATIONS

In order to find the relationship between the confidence measure  $C$  defined in (4) and the displacement estimation errors expressed by the root-mean-square-error  $\delta_{\Delta \hat{\mathbf{u}}}$  (see also (12)) of the 2D displacement estimator described in section 2.1, detailed statistical investigations were carried out using simulated ultrasound echo signals from strained software-phantoms. The goal of these simulations is to determine analytic functions to be then used for the calculation of  $\delta_{\Delta \hat{\mathbf{u}}}$  from the confidence measure  $C$ .

### 3.1 SIGNAL GENERATION

Synthetic ultrasound echo signals were generated for strained software-phantoms containing  $k = 1 \dots K$  point scatterers, each of which being defined by its 3D position  $\mathbf{x}_k$  and a factor  $-1 \leq R_k \leq +1$  representing the individual amplitude contribution to the echo signals. Different values of uniaxial strain  $\varepsilon_{zz} = \partial u_z / \partial z$  in the range of 0.5% to 4% were applied in 0.5% steps to the  $K$  scatterer positions using the following simplified elasto-mechanical model:

$$\mathbf{x}_{k,\varepsilon_{zz}} = \mathbf{x}_k \cdot \begin{pmatrix} 1 - \nu \cdot \varepsilon_{zz} & 0 & 0 \\ 0 & 1 - \nu \cdot \varepsilon_{zz} & 0 \\ 0 & 0 & 1 + \varepsilon_{zz} \end{pmatrix} \quad (17)$$

where the *Poisson's ratio*  $\nu$  was chosen to be 0.495 (virtually incompressible soft tissue).

The echo signals from the homogenous software-phantoms were generated with ultrasonic pulse properties listed in Tab. 1 in order to emulate the characteristics of the ultrasound transducer (linear array) and scanner used for the experimental data acquisition. Frequency-dependent attenuation was not taken into consideration.

Table 1: Echo signal parameters: center frequency  $f_c$ ; relative FWHM bandwidth  $B_r$ ; axial  $\ell_{R,z}$ , lateral  $\ell_{R,x}$  and elevational  $\ell_{R,y}$  auto-correlation lengths. Simulation results shown in this paper are based on the sampling frequency  $f_s$  of the applied ultrasound scanner VOLUSON 730 (GE Kretztechnik) which is equipped with a digital research interface in order to access the beamformed radio-frequency echo data.

$f_c$ MHz	$B_r$ %	$\ell_{R,z}$ $\mu\text{m}$	$\ell_{R,x}$ $\mu\text{m}$	$\ell_{R,y}$ $\mu\text{m}$	$f_s$ MS/s
7.82	47	175	309	558	30

The following process was implemented in order to derive statistically meaningful results: echo signals at 16 laterally adjacent parallel lines of sight (LOS) were generated for different compression steps (i.e. strain values) and for a large number of realizations of the software-phantom. The boundary conditions at the top and bottom surfaces of the phantom were assumed to be "free slip". The LOS were symmetrically aligned around the lateral (and elevational) symmetry axes ( $x = 0 \mu\text{m}$ ,  $y = 0 \mu\text{m}$ ) of the software-phantom with the same pitch ( $100 \mu\text{m}$ ) of the later applied linear array transducer, such that the mean displacements within a centered template block in lateral (and elevational) direction is zero. This simulation set-up allows the detailed investigation of signal decorrelation effects due to compression independently from a lateral (and elevational) net displacement of the template block. To quantify the axial displacement estimation errors due to lateral displacements induced by the (uni-)axial compression, various rigid lateral displacements  $u_x$  in the range of  $\pm 50 \mu\text{m}$  (i.e.  $\pm 0.5$  LOS) were applied to the phantom (see Tab. 2). In this paper we limit the presentation of results to the situation with zero-mean elevational displacement inside the template block and focus on those estimation errors that are caused by (uni-)axial compressions as well as the associated lateral displacements.

Table 2: Values of axial strain  $\varepsilon_{zz}$  and lateral displacement  $u_x$  applied to the software-phantoms. Different SNR levels were generated by adding zero-mean white Gaussian noise to the echo signals.

	Value	Unit
$\varepsilon_{zz}$	0 : 0.5 : 4.0	%
$u_x$	-50 : 5 : 50	$\mu\text{m}$
SNR	40,35,30,25,20,18,16,14,12,10,8,6	dB

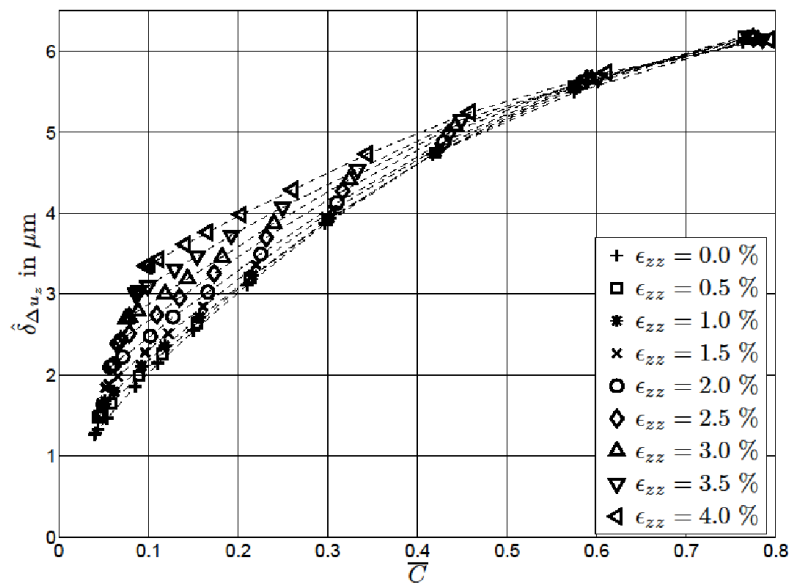
### 3.2 DISPLACEMENT ESTIMATION RESULTS

The 2D displacement estimation described in section 2.1 was carried out on the echo signal envelopes  $A[m,n]$  and  $A'[m,n]$ , which were calculated from the noisy synthetic radio-frequency (RF) echo signals  $s_e[m,n]$  and  $s'_e[m,n]$  using the Hilbert transform [24]. A template-block-size  $T[k,\ell]$  of 24 samples x 12 samples (approx. 600  $\mu\text{m}$  axially x 1200  $\mu\text{m}$  laterally) was chosen, which was found in earlier investigations [21] to be the best choice for typical situations and parameters.

The displacement estimation errors  $\Delta u_z = \hat{u}_z - u_z$  (axial) and  $\Delta u_x = \hat{u}_x - u_x$  (lateral) of the displacement estimates  $\hat{u}_z$  and  $\hat{u}_x$  were derived using the true displacements  $u_z$  and  $u_x$ , which in turn were deduced from (17) for the center position of each template block  $T[k,\ell]$ . The root-mean-square (RMS) displacement errors  $\hat{\delta}_{\Delta u_z}$  and  $\hat{\delta}_{\Delta u_x}$  (including estimation bias and estimation variance) derived from  $N$  displacement estimates (shown here only for  $\Delta u_z$ )

$$\hat{\delta}_{\Delta u_z} = \sqrt{\frac{1}{N} \sum_{n=1}^N (\hat{u}_z - u_z)^2} \tag{18}$$

are shown in Fig. 3 as a function of the confidence measure  $C$  for different values of axial strain  $\epsilon_{zz}$ , where the confidence measure in fact corresponds to the mean value  $\bar{C}$  of  $C$  defined in (4).  $\bar{C}$  was calculated from all 2D displacement estimates in the lateral range  $-50 \mu\text{m} \leq u_x \leq +50 \mu\text{m}$  and the respective echo SNR levels (range: 40 to 6 dB) that occur at the corresponding depth locations. As a result, the  $\bar{C}$ -value of each data point in Fig. 3 represents a particular SNR level.



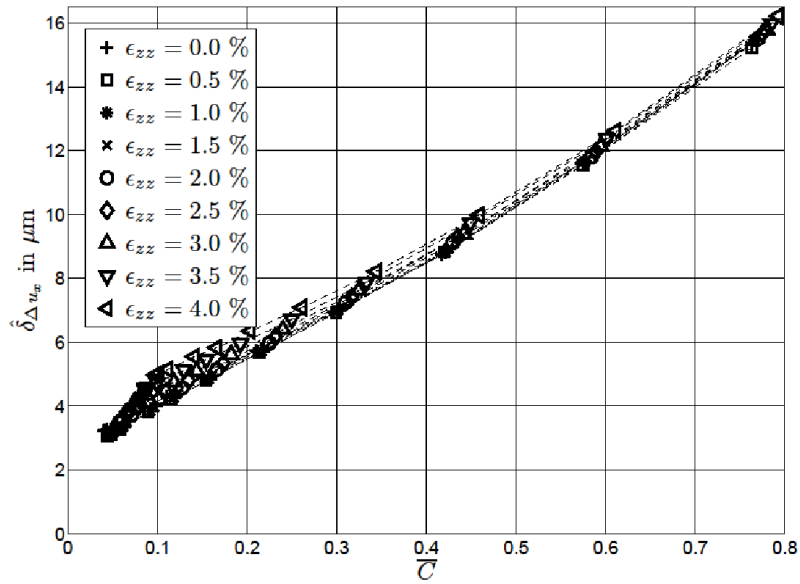


**Fig. 3.** RMS displacement errors  $\hat{\delta}_{\Delta U_Z}$  (top) and  $\hat{\delta}_{\Delta U_X}$  (bottom) as a function of the confidence measure  $\bar{C}$  for different values of  $\varepsilon_{zz}$  (depicted here for  $u_y = \text{const.} = 0 \mu\text{m}$ ). If  $u_y \neq 0$  microns (not shown), the values for  $\hat{\delta}_{\Delta U_Z}$  and  $\hat{\delta}_{\Delta U_X}$  increase and their dependence on  $\bar{C}$  is less strongly pronounced compared to  $u_y = \text{const.} = 0 \mu\text{m}$ .

It can be easily seen that the strain value  $\varepsilon_{zz}$  does not appreciably influence  $\hat{\delta}_{\Delta U_Z}$  as a function of  $\bar{C}$ . However, the relation between  $\hat{\delta}_{\Delta U_Z}$  and lower values of  $\bar{C}$  more strongly depends on  $\varepsilon_{zz}$ , and thus a single analytic approximation for this relation does not exist. However, in most practical cases of static ultrasound elastography the mean strain value within certain regions of interest (ROI) might be applicable as a good approximation. Thus, analytical representations (cubic fits) for different values of  $\varepsilon_{zz}$  were implemented for  $\hat{\delta}_{\Delta U_Z}$  as well as for  $\hat{\delta}_{\Delta U_X}$  as functions of  $\bar{C}$ :

$$\begin{aligned} f_{\hat{\delta}_{\Delta U_Z}}(\bar{C}) &= a_{z,0} + a_{z,1} \bar{C} + a_{z,2} \bar{C}^2 + a_{z,3} \bar{C}^3 \\ f_{\hat{\delta}_{\Delta U_X}}(\bar{C}) &= a_{x,0} + a_{x,1} \bar{C} + a_{x,2} \bar{C}^2 + a_{x,3} \bar{C}^3 \end{aligned} \quad (19)$$

The coefficients  $a_{z,1}$  to  $a_{z,3}$  and  $a_{x,1}$  to  $a_{x,3}$  were determined in a least-squares sense from the data shown in Fig. 3. Estimates of the root-mean-square (RMS) displacement errors for each and every displacement estimate can be now calculated individually from their respective confidence measure  $\bar{C}$  using the analytical approximations  $f_{\hat{\delta}_{\Delta U_Z}}(\bar{C})$  and  $f_{\hat{\delta}_{\Delta U_X}}(\bar{C})$ . These RMS displacement errors are then used to calculate the adaptive weight factors  $W$  for the E-modulus reconstruction as shown in the next section.

## 4 EXPERIMENTAL RESULTS

Based upon the promising simulation results already published in [1], we performed compressions experiments on self-made agar phantoms in order to evaluate the proposed reconstruction approach in practice with experimental echo data.

### 4.1 EXPERIMENTAL SETUP AND DATA ACQUISITION

The experimental setup for the data acquisition from a uniaxially compressed ultrasound phantom with a soft(er) homogeneous background and 3 hard(er) cylindrical inclusions is shown in Fig. 4. The self-made phantom was made of agar-

agar with cornstarch as additional scatterers [25]. Indentor measurements [26] using samples with particular geometry of the phantom material (8 independent measurements) yielded E-modulus values for the homogenous background of  $E_B = 92.0 \pm 1.0$  kPa and for the cylindrical inclusions of  $E_I = 254 \pm 5.1$  kPa. The phantom was placed between two parallel compressions plates (also made of agar-agar,  $E_C = 390 \pm 13.5$  kPa) with a moderate pre-compression mainly in order to avoid that ultrasonic reverberations lie inside the region of interest. A TPX<sup>®</sup> [27] plate of 1 mm thickness was flush mounted to the upper polycarbonate plate in order to ensure stable conditions during compression and avoid the bending of the phantom material into the acoustic window. Before and after small compression steps applied to the phantom by lifting it with an automated elevational table controlled by LabVIEW<sup>®</sup> from below against the fixed upper polycarbonate plate, digital RF echo data were acquired through the acoustic window using a linear array transducer attached to the VOLUSON 730 ultrasound scanner with settings typical for breast ultrasound examinations.

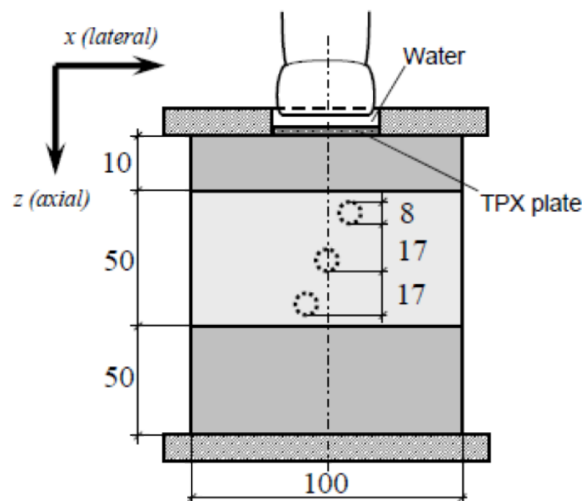


**Fig. 4. Experimental setup: the ultrasound transducer acquires echo signals through an acoustic window (1 mm TPX<sup>®</sup> plate) in the upper polycarbonate compression plate from an agar-agar phantom (100 mm x 100 mm x 50 mm) with 3 hard cylindrical inclusions of 8 mm diameter each at different uniaxial compression steps applied from below by an elevational table. Two stiff plates also made of agar-agar were used in order to avoid that strong reverberations occur in the region of interest. All measures are given in mm.**

#### 4.2 DISPLACEMENT ESTIMATION

2D displacement estimates were calculated from the acquired echo signals with the algorithm described in section 2.1 using a template block size of 24 samples x 12 samples  $\approx 600 \mu\text{m} \times 1200 \mu\text{m}$  (axial x lateral). A lateral block-overlap of 50% was applied in order to achieve the same spatial resolutions in axial and lateral direction. Consequently,  $I \times J$  2D displacement vector estimates  $\hat{u}[i,j]$  are available on the rectangular grid with a mesh size of approximately  $600 \mu\text{m} \times 600 \mu\text{m}$ .

In Fig. 5 the spatial distributions of the axial  $\hat{u}_z$  (left) and lateral  $\hat{u}_x$  (right) components of  $\hat{u}[i,j]$  are illustrated. The horizontal dashed lines indicate the upper ( $z = 15.6$  mm) and lower ( $z = 58.2$  mm) boundaries of the phantom. Within the region of approximately  $42.6$  mm x  $31.2$  mm inside the phantom,  $73 \times 52$  2D displacement vector estimates  $\hat{u}[i,j]$  are available for the E-modulus reconstruction.

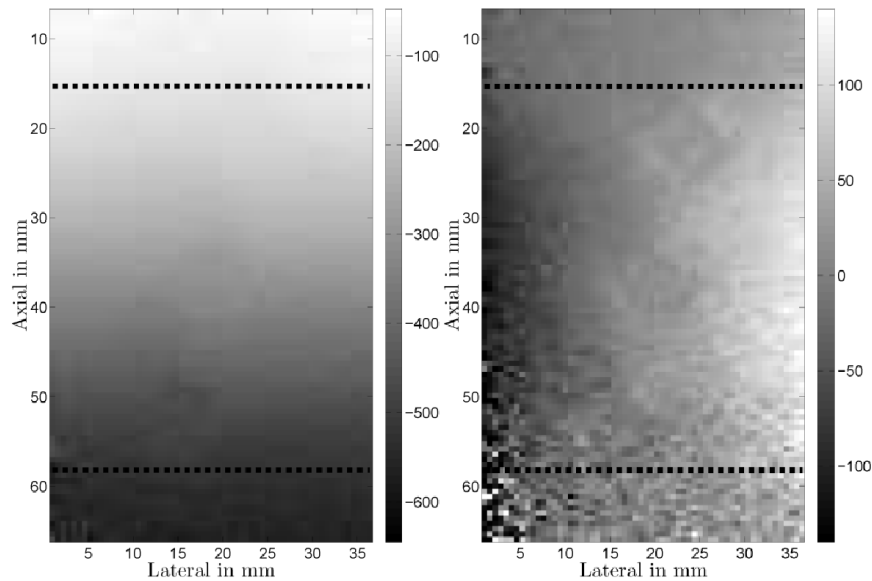


**Fig. 5.** Spatial distributions of the axial  $\hat{u}_z$  (left) and lateral  $\hat{u}_x$  (right) components of the 2D displacement vector estimates  $\hat{u}[i, j]$  for an applied strain of 1%. The horizontal dashed lines indicate the upper and lower boundaries of the phantom. Color maps are in  $\mu\text{m}$ .

In Fig. 6 the spatial mean echo SNR of the acquired signals within laterally centered regions of 2.5 mm x 32 mm (axial x lateral) and 50% axial overlap as well as the mean values  $\bar{C}$  of the confidence measure  $C$  for all 52 lateral displacement estimates are shown as a function of depth  $z$  (axial) inside the phantom ( $15.6 \text{ mm} \leq z \leq 58.2 \text{ mm}$ ). Each SNR value was estimated from 400 independent realizations of the echo signals.

Within the first 15 mm in the phantom, the SNR remains relatively constant at approx. 30 dB. The slight increase at approx. 25 mm depth is due to the focal length setting. For  $z > 30 \text{ mm}$  a virtually linear decrease of the echo SNR occurs, with a degradation of the SNR value down to 9 dB at the bottom of the phantom (at  $z \approx 58 \text{ mm}$ ). It can be seen that  $\bar{C}$  - similar to the echo SNR - remains relatively constant at a value of approximately 0.1 in the axial range  $15 \text{ mm} \leq z \leq 30 \text{ mm}$ . For  $z > 30 \text{ mm}$ ,  $\bar{C}$  steadily increases to a value of approximately 0.65 due to the rising displacement estimation errors.

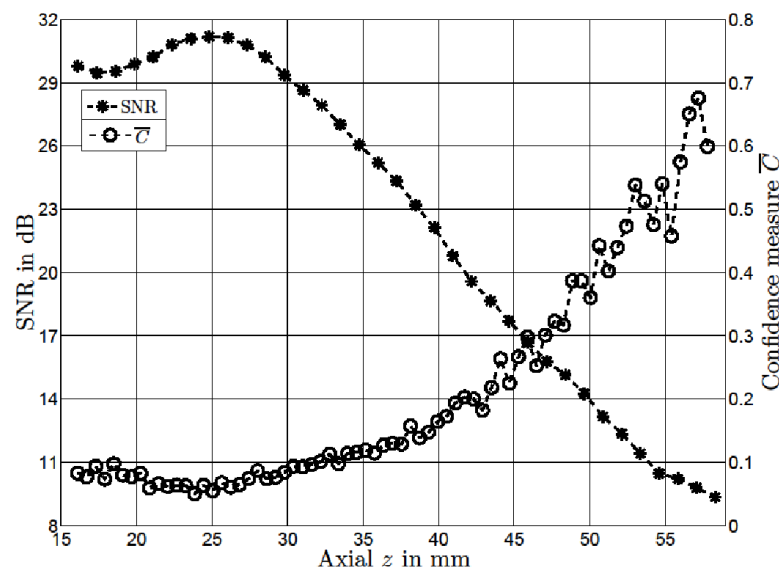


**Fig. 6.** SNR in dB of the echo signals acquired from the phantom and mean value  $\bar{C}$  of the confidence measure  $C$  of all 52 lateral displacement estimates in the phantom as a function of depth  $z$  (axial).

### 4.3 E-MODULUS RECONSTRUCTION

As described in section 2.2, the true spatial E-modulus distribution was modeled as a spatially piecewise constant function  $E[m,n]$  on the same rectangular grid as used for the displacement estimation (mesh size  $h_z = h_x = 600 \mu\text{m}$ ). For the reconstruction, Dirichlet boundary conditions were chosen for  $F$  (see (10)) from the estimated displacements  $\hat{\mathbf{u}}[i,j]$  at the upper and the lower boundaries of the phantom. The assigned displacement values were those from the first ( $i = 1$ ) and the last ( $i = 73$ ) row of  $\hat{\mathbf{u}}[i,j]$ , see dashed lines in Fig. 5. On the left and right boundaries of the phantom Neumann boundary conditions were chosen for  $F$  (see (10)) with  $\sum_{j=1}^2 \sigma_{ij} \cdot n_j = 0$ , i.e. no external forces occur, where  $\sigma_{ij}$  and  $n_j$  denote the mechanical stress tensor and the outward normal vector on the boundary edge, respectively. The E-modulus reconstruction model comprises  $71 \times 52$  ( $I \times J$ ) displacement values/nodes  $\mathbf{u}[i,j]$ , and thus  $70 \times 50$  ( $M \times N$ ) E-modulus nodes  $E_\rho[m,n]$  on a rectangular region  $\Omega$  of size  $42 \times 30 \text{ mm}^2$  ( $\ell_z \times \ell_x$ ).

The reconstruction process was then carried out by approximately solving (15) using  $\hat{\mathbf{u}}[i,j]$  and different values of the regularization coefficient  $\rho$  (see also Fig. 2). The weight factors  $W_1[i,j] = [W_{1,z}, W_{1,x}]^T$  for the individual displacement estimates  $\hat{\mathbf{u}}[i,j]$  were determined using (12). The RMS errors  $\hat{\delta}_{\Delta u_z}$  and  $\hat{\delta}_{\Delta u_x}$  were derived from the values of  $\bar{C}$  using  $f_{\delta_{\Delta u_z}}(\bar{C})$  and  $f_{\delta_{\Delta u_x}}(\bar{C})$  from (19). For reasons of comparison, the reconstructions were also carried out with spatially ( $[i,j]$ ) constant weight factors  $W_2[i,j] = [W_{2,z}, W_{2,x}]^T$ . Based on the fact that the displacement estimation errors in lateral direction are approximately  $\approx 1.7$  times larger than those in axial direction,  $W_2[i,j] = [W_{2,z}, W_{2,x}]^T = [1; 1/1.7]^T$  was applied. The indices of the two-dimensional quantities  $\hat{\mathbf{u}}[i,j]$ ,  $W_1[i,j]$  and  $W_2[i,j]$  were linearized to  $\hat{\mathbf{u}}[p]$ ,  $W_1[p]$  and  $W_2[p]$  with  $p = i + I \cdot (j - 1)$ , such that (15) can be applied.

In Fig. 7, the weight factors  $W_{1,z}$ ,  $W_{1,x}$ ,  $W_{2,z}$  and  $W_{2,x}$  of the axial and lateral displacement estimates are shown as function of the axial depth  $z$ . The existing increase of the displacement estimation errors with  $z$  leads to a decrease of the weight factors  $W_{1,z}$  and  $W_{1,x}$  down to values of approximately 0.2-0.3. Recall, that a local decrease of weight factors will lead to a local increase of regularization in the reconstructed elastogram. This effect will be demonstrated in section 4.4.

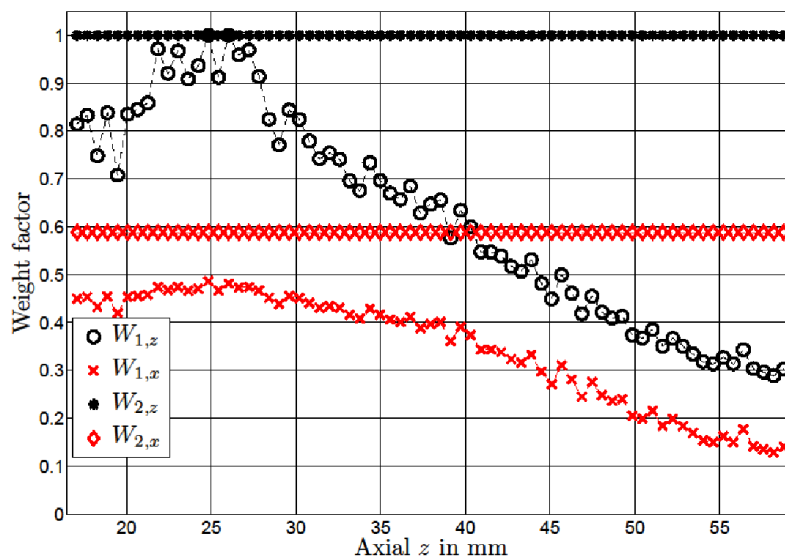
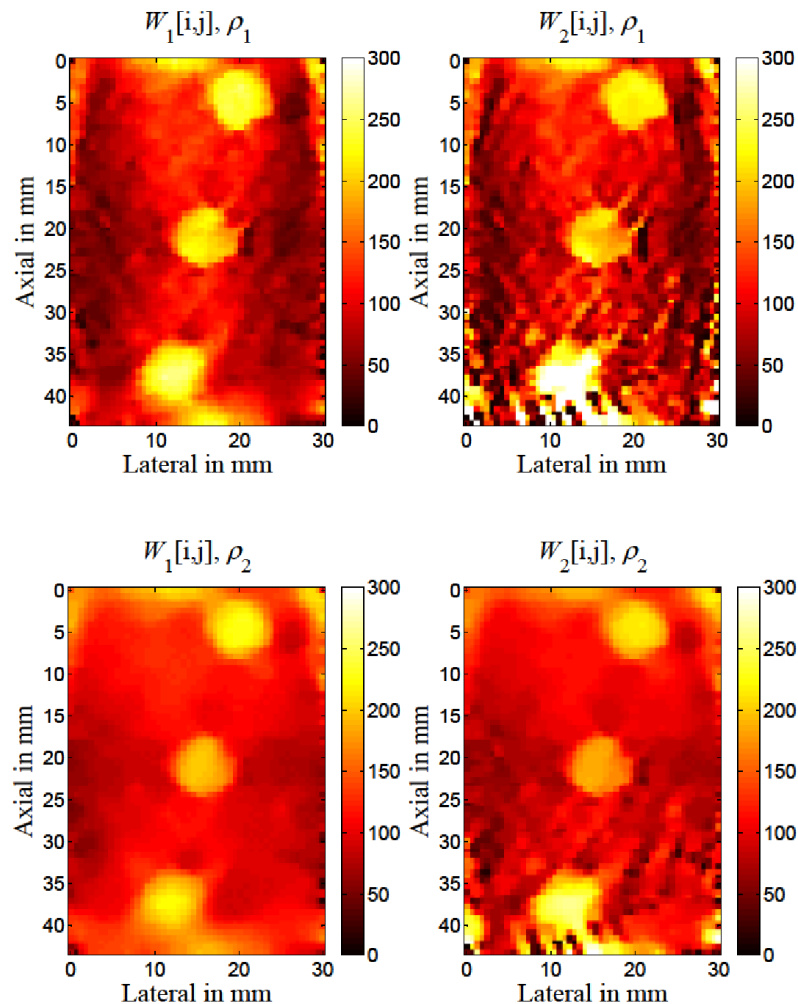


Fig. 7. Adaptive weight factors  $W_1 = [W_{1,z}, W_{1,x}]$  and constant weight factors  $W_2 = [W_{2,z}, W_{2,x}]$  used for the reconstruction depicted as a function of axial depth  $z$ .

#### 4.4 RECONSTRUCTION RESULTS

Reconstructed elastograms are depicted in Fig. 8 for two different regularization coefficients  $\rho_1 : \rho_2 = 1 : 3.6$  when either the adaptive weight factors  $W_1[i,j]$  or the spatially constant weight factors  $W_2[i,j]$  are applied. For demonstration purposes, the regularization coefficients  $\rho_1$  and  $\rho_2$  were determined such that in the reconstructed elastograms the best visual differentiation between the background and inclusions exists when using  $W_1[i,j]$  and  $W_2[i,j]$ , respectively. It specifically needs to be pointed out here, that Fig. 8 depicts the “raw” reconstruction data, i.e. neither the displacement estimates nor the reconstructed elastograms were filtered, averaged or “visually improved” in any kind.

For the smaller regularization coefficient  $\rho_1$  (i.e. low(er) degree of regularization), the increasing displacement estimation errors towards the bottom regions lead to significant artifacts (under-regularization) in the reconstructed elastogram when constant weight factors  $W_2[i,j]$  are used. However, the reconstructed elastogram for the adaptive weight factors  $W_1[i,j]$  appears sufficiently regularized even at the bottom regions. For the larger regularization coefficient  $\rho_2$  (i.e. higher degree of regularization) the elastograms for both weight factors  $W_1[i,j]$  (adaptive) and  $W_2[i,j]$  (constant) appear to be sufficiently regularized (with some advantages with regard to the bottom regions when applying the adaptive weight factors). However, in both cases ( $W_1[i,j]$  and  $W_2[i,j]$ ) the spatial resolution is worse compared to the reconstruction results obtained with the smaller regularization coefficient  $\rho_1$ . The effects of over-regularization are most clearly pronounced at the edges between the background and the inclusion(s), which are more difficult to define in structure and size when  $\rho_2$  is applied. It can be concluded from the visual appearance of the elastograms that the use of adaptive weight factors  $W_1[i,j]$  and an appropriate regularization coefficient results in a superior quality of the reconstructed elastograms.



**Fig. 8.** Reconstruction results  $E_p[m,n]$  using displacement estimates derived from experimental ultrasound echo data for adaptive weight factors  $W_1[i,j]$  (left column) and constant weight factors  $W_2[i,j]$  (right column) and the two “best” values of  $\rho$  (see text).

In order to compare the quality of the reconstructed elastograms on a quantitative basis, the two measures “contrast” and “background homogeneity” were used. The elastogram contrast

$$C_I = \frac{\bar{E}_{\rho,I}}{\bar{E}_{\rho,B}} \cdot \tag{20}$$

of the 3 inclusions ( $\bar{E}_{\rho,I}$ ) and the background ( $\bar{E}_{\rho,B}$ ) was calculated for the reconstruction results  $E_\rho$  shown in Fig. 8. The respective mean values  $\bar{E}_{\rho,B}$  and  $\bar{E}_{\rho,I}$  were derived from the elastograms for 3 equally-sized “depth regions” (indicated by the 2 dashed straight lines in Fig. 9) each of which comprises one inclusion. According to the indenter measurements performed using samples of the inclusion and background materials (see also section 4.1), the (true) contrast is  $C_I = 254 \text{ kPa}/92 \text{ kPa} = 2.8$ .

In order to quantify the background homogeneity, the empirical standard deviation  $\sigma_{E_{\rho,B}}$  of  $E_\rho$  was calculated inside the 3 background regions shown in Fig. 9. This measure might be also of diagnostic importance since a small inclusion even at a large contrast can be easily overlooked in a reconstructed elastogram with spatially (too) inhomogeneous background.

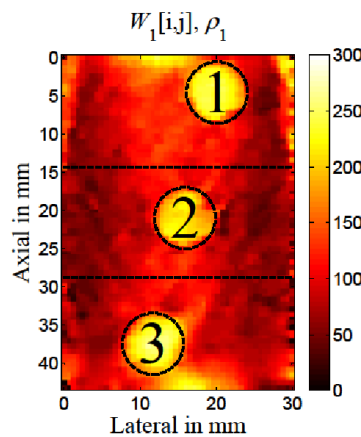


Fig. 9. Reconstructed elastogram  $E_\rho[m,n]$  for  $W_1[i,j]$  and  $\rho_1$  also shown in Fig. 8.

The dashed lines and circles indicate the 3 regions of E-modulus nodes inside which the spatial mean values  $\bar{E}_{\rho,B}(\sigma_{E_{\rho,I}})$  and  $\bar{E}_{\rho,I}$  were calculated.

In Tab. 3 the values of  $\sigma_{E_{\rho,B}}$  and  $C_I$  are shown for all 3 regions when using either  $W_1[i, j]$  or  $W_2[i, j]$  and for both values  $\rho_1$  and  $\rho_2$  of the reconstruction coefficient. The contrast  $C_I$  in all 3 regions is higher - for both  $W_1[i, j]$  and  $W_2[i, j]$  - when the smaller regularization coefficient  $\rho_1$  is used. With an increasing elastogram contrast that approaches the true value, the homogeneity of the in fact completely homogenous background significantly degrades. This degradation expressed by an increase in  $\sigma_{E_{\rho,B}}$  is much less pronounced when the adaptive weight factors  $W_1[i,j]$  instead of the constant weight factors  $W_2[i,j]$  are applied. For example,  $\sigma_{E_{\rho,B}}$  in region 3 with  $W_1[i,j]$  is less than half (38.4 kPa) of the value (80.5 kPa) obtained with  $W_2[i,j]$ . This can also be (visually) observed in Fig. 8.

Table 3: Values of  $\sigma_{E,\rho,B}$  and  $C_i$  for the 3 regions (each of which with one cylindrical inclusion) and the 2 values of  $\rho$ . The true value for  $C_i$  is 2.76, the best value for  $\sigma_{E,\rho,B}$  is 0.

Inclusion #	$\rho$	$\sigma_{E,\rho,B}$ in kPa		$C_i$	
		$W_1[i,j]$	$W_2[i,j]$	$W_1[i,j]$	$W_2[i,j]$
1	$\rho_1$	40.3	42.9	1.8	1.8
	$\rho_2$	27.0	26.9	1.5	1.5
2	$\rho_1$	26.2	32.6	2.4	2.3
	$\rho_2$	15.4	15.8	1.8	1.8
3	$\rho_1$	38.4	80.5	2.2	2.4
	$\rho_2$	27.1	48.9	1.7	2.0

In Fig. 10 the reconstructed elastogram for  $\rho_1$  and  $W_1[i,j]$  is directly compared to a conventional strain image (axial strain). The strain image was derived from the same axial displacement estimates that were used for the E-modulus reconstruction by applying a least-squares strain filter with 11 filter taps as described in [13].

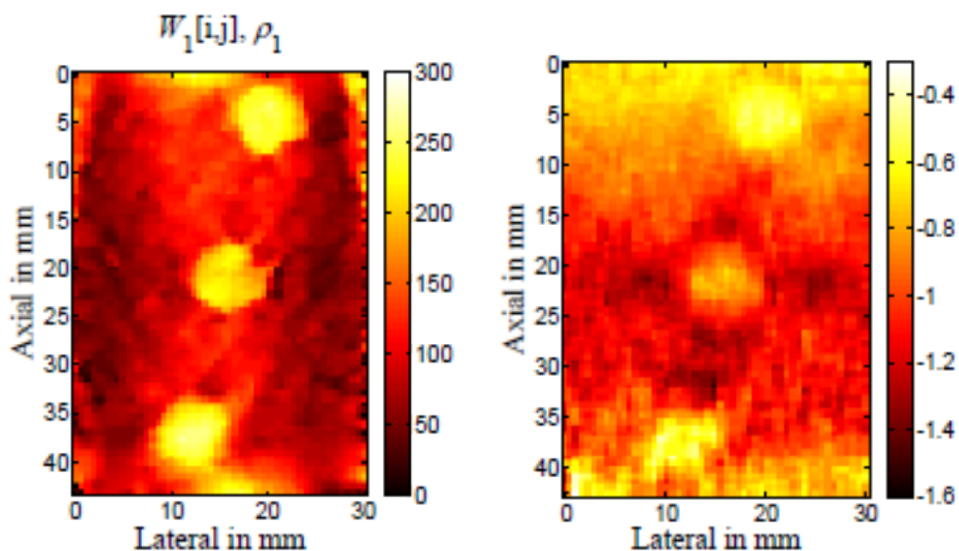


Fig. 10. Left: reconstructed E-modulus distribution  $E_\rho[m, n]$  when using  $\rho_1$  and  $W_1[i, j]$ . Right: corresponding conventional image of the axial strain derived from the same displacement data. The applied strain is 1.0 %, the color maps are scaled in kPa (left) and % (right).

The superior quality of the reconstructed elastogram is obvious. While the reconstructed elastogram clearly depicts all 3 inclusions on a relatively homogenous background, the strain image is not quite as clear: inclusions 1 and 3 are difficult to (diagnostically) assess, and even in the region with inclusion 2 a rather low strain contrast exists.

## 5 CONCLUSIONS

In elastography, internal tissue displacements must be estimated. The unavoidable displacement estimation errors are governed by the applied estimator, the ultrasound imaging parameters, and the coherence of the (digital) echo signals; the latter is influenced by tissue compression and noise. Depending on the displacement estimation method, the estimation errors might also depend on the displacement value (e.g. with full-sample displacement cyclo-stationarity). Since the signal-to-noise ratio in the field-of-view (FOV) is spatially non-stationary, the displacement estimation errors are also of non-

stationary character. As a result, the displacement estimation errors are always spatially dependent within the ultrasonic field-of-view.

E-modulus reconstruction processes applicable in practice most often employ regularization. If the amount of regularization is too small (under-regularization), a loss of homogeneity in regions with in fact homogenous E-modulus distribution occurs. If the amount of regularization is too large (over-regularization), diagnostically important high-frequency spatial information is lost. The optimal amount of regularization strikes the best balance between these two opposing effects and provides the best elastogram quality possible.

The conventional approach to solve the inverse problem is to apply equal regularization to the entire FOV, i.e. using (spatially) constant weight factors  $W_2[i, j] = \text{const}$ . As we have demonstrated for a typical breast elastography situation, this approach inevitably leads to under- and over-regularization in different depth regions of the FOV at the same time. The approach proposed in this paper applies (spatially) adaptive weight factors  $W_2[i, j]$ , which are derived from the mean square displacement estimation errors by means of an appropriate confidence measure  $C$ . As a result, over- and under-regularization at the top and bottom regions within the FOV are significantly reduced because the weight factors are adapted as a function of depth. This leads to superior E-modulus reconstruction results and elastogram quality that might help improve the diagnostic value of ultrasound elastography. An even more sophisticated - but computationally also more expensive - approach that we currently investigate is to fully adapt the weight factors in both, the axial and lateral directions.

## REFERENCES

- [1] A. Eder, M. Richter, and Ch. Kargel. A new approach to improve the reconstruction quality in ultrasound elastography. In *International Instrumentation and Measurement Technology Conference (I2MTC 2012)*, Graz, Austria, May 2012.
- [2] P. P. Rosen. *Rosen's breast pathology*. Lippincott Williams & Wilkins, Philadelphia, 2nd edition, 2001.
- [3] J. Ophir, I. Céspedes, H. Ponnekanti, Y. Yazdi, and X. Li. Elastography: a method for imaging the elasticity of biological tissues. *Ultrason. Imag.*, 13:111-134, 1991.
- [4] T.J. Hall, Y. Zhu, C.S. Spalding, and L.T. Cook. In vivo real-time freehand elasticity imaging. *Ultrasound Med. Biol.*, 29(3):427-35, 2003.
- [5] K. Nightingale, M. Palmeri, R. Nightingale, and G. Trahey. On the feasibility of remote palpation using acoustic radiation force. *J. Acoust. Soc. Am.*, 110(1):625-634, 2001.
- [6] A.P. Sarvazyan, O.V. Rudenko, S.D. Swanson, J.B. Fowlkes, and S.Y. Emilianov. Shear wave elasticity imaging: a new ultrasonic technology of medical diagnostics. *Ultrasound Med. Biol.*, 24(9):1419-1435, 1998.
- [7] T. Elgeti, J. Rump, U. Hamhaber, S. Papazoglou, B. Hamm, J. Braun, and I. Sack. Cardiac Magnetic Resonance Elastography: Initial Results. *Investigative Radiology*, 43:762-772, 2008.
- [8] J.-L. Gennisson, T. De\_eux, M. Fink, and M. Tanter. Ultrasound elastography: Principles and techniques. *Diagnostic and interventional imaging*, 94:487-495, 2013.
- [9] A. Pesavento, C. Perrey, M. Krueger, and H. Ermert. A time-efficient and accurate strain estimation concept for ultrasonic elastography using iterative phase zero estimation. *IEEE Trans. Ultrason. Ferroelectr. Freq. Control*, 46(5):1057-67, Sept. 1999.
- [10] T.J. Hall and J. Jiang. Motion tracking for palpation imaging. In *IEEE International Symposium on Biomedical Imaging: From Macro to Nano*, volume 1, pages 45-48, 2004.
- [11] M.S. Richards, P.E. Barbone, and A.A. Oberai. Quantitative three-dimensional elasticity imaging from quasi-static deformation: a phantom study. *Phys. Med. Biol.*, 54:757-779, 2009.
- [12] A. Eder, T. Arnold, and Ch. Kargel. Performance Evaluation of Displacement Estimators for Real-Time Ultrasonic Strain and Blood Flow Imaging with Improved Spatial Resolution. *IEEE Trans. Instr. Meas.*, pages 1275-84, September 2007.
- [13] F. Kallel and J. Ophir. A Least-Squares Strain Estimator for Elastography. *Ultrason. Imag.*, 19:195-208, 1997.
- [14] E. Hayes. Elastography stretches horizons of breast ultrasound. *Diagn. Imaging*, pages 43-44, 2006.
- [15] M.M. Doyley, S. Srinivasan, S. Pendergrass, Z. Wu, and J. Ophir. Comparative evaluation of strain-based and model-based modulus elastography. *Ultrasound Med. Biol.*, 31:787-802, 2005.
- [16] L.D. Landau and E.M. Lifshitz. *Theory of Elasticity*, volume 7 of *Course of Theoretical Physics*. Elsevier Ltd., 3 edition, 1986.
- [17] F. Kallel and M. Bertrand. Tissue Elasticity Reconstruction Using Linear Perturbation Method. *IEEE Trans. Med. Imag.*, Vol. 15(No. 3):299-313, June 1996.
- [18] A.A. Oberai, N.H. Gokhale, and G.R. Feijoo. Solution of Inverse Problems in Elasticity Imaging Using the Adjoint Method. *Inverse Problems*, 19:297-313, 2003.

- [19] J. Li, Y. Cui, M. Kadour, and J.A. Noble. Elasticity Reconstruction from Displacement and Confidence Measures of a Multi-compressed Ultrasound RF Sequence. *IEEE Trans. Ultrason. Ferroelectr. Freq. Control*, 55(2):319-326, Feb. 2008.
- [20] T.J.R. Hughes. *The Finite Element Method*. Prentice-Hall, Inc., 1987.
- [21] A. Eder and Ch. Kargel. 2D-Echtzeit-Ultraschallverfahren zur Messung der Gewebeelastizität für die Tumorfrüherkennung. *Technisches Messen (TM)*, 76(6):283-291, 2009.
- [22] W.H. Press, S.A. Teukolsky, W.T. Vetterling, and B.P. Flannery. *Numerical Recipes: The Art of Scientific Computing*. Cam, 3rd edition, 2007.
- [23] A. Rieder. *Keine Probleme mit Inversen Problemen*. Vieweg, Wiesbaden, 1 edition, 2003.
- [24] A.V. Oppenheim, R.W. Schaffer, and J.R. Buck. *Discrete-Time Signal Processing*. Prentice-Hall, Inc., New York, 2 edition, 1999.
- [25] Ch. Kargel, G. Plevnik, J. Mai, B. Trummer, C. Pellot-Barakat, and M.F. Insana. Ultrasonic Strain Flow Imaging. In *Ultrason*. Int. Technical University of Delf, The Netherlands, Elsevier Science, 2001.
- [26] Ch. Kargel, B. Trummer, G. Plevnik, C. Pellot-Barakat, J.J. Mai, and M.F. Insana. Is Ultrasonic Imaging a sensitive Indicator of spatially varying elastic anisotropy? In *IEEE Int. Ultrason. Symp.*, Atlanta, GA, 2001.
- [27] Mitsui Chemicals, Inc., Shiodome City Center, 5-2, Higashi Shimbashi 1-chome, Minato-ku, Tokyo 105-7117, Japan. *Polymethyl Pentene (PMP) TPX<sup>TM</sup>*.